Supporting Information

Arbitrary-Shaped Graphene-Based Planar Sandwich Supercapacitors on One Substrate with Enhanced Flexibility and Integration

Shuanghao Zheng[†,‡,§], Xingyan Tang[‖], Zhong-Shuai Wu[†,], Yuan-Zhi Tan[‖], Sen Wang[†,‡], Chenglin Sun[†], Hui-Ming Cheng[#,¥], Xinhe Bao[†,§]*

[†] Dalian National Laboratory for Clean Energy, Dalian Institute of Chemical Physics, Chinese Academy of Sciences, 457 Zhongshan Road, Dalian 116023, China

[‖] State Key Laboratory for Physical Chemistry of Solid Surfaces and Department of Chemistry, College of Chemistry and Chemical Engineering, Xiamen University, 422 Siming South Road, Xiamen, 361005, China

[§] State Key Laboratory of Catalysis, Dalian Institute of Chemical Physics, Chinese Academy of Sciences, 457 Zhongshan Road, Dalian 116023, China

[‡] University of Chinese Academy of Sciences, 19 A Yuquan Rd, Shijingshan District, Beijing, 100049, China

[#] Shenyang National Laboratory for Materials Science, Institute of Metal Research, Chinese Academy of Sciences, 72 Wenhua Road, Shenyang 110016, P. R. China

[¥] Tsinghua-Berkeley Shenzhen Institute (TBSI), Tsinghua University, 1001 Xueyuan Road, Shenzhen 518055, P. R. China

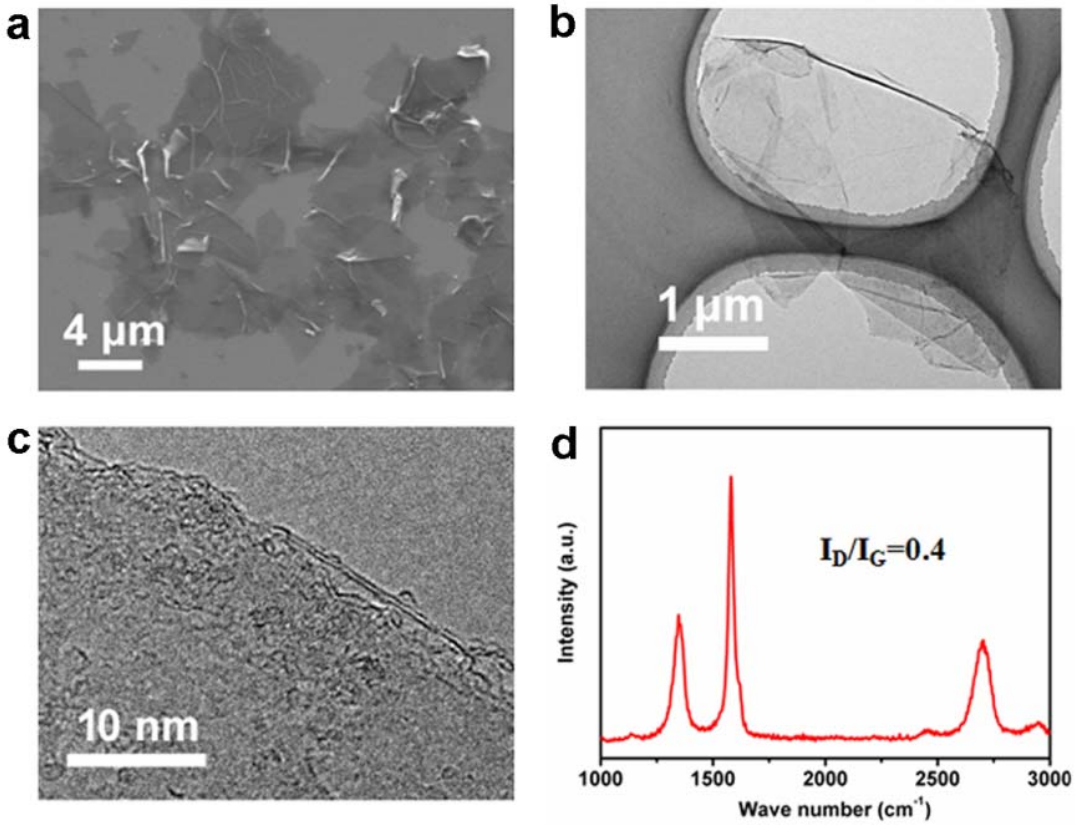

Figure S1. The characterization of EG nanosheets. (a) SEM image, and (b) TEM image, showing the flat and uniform morphology. (c) HRTEM image, showing a double-layer structure. (d) Raman spectrum of EG with a low intensity ratio (0.4) of I_D/I_G, indicative of high-quality graphene.

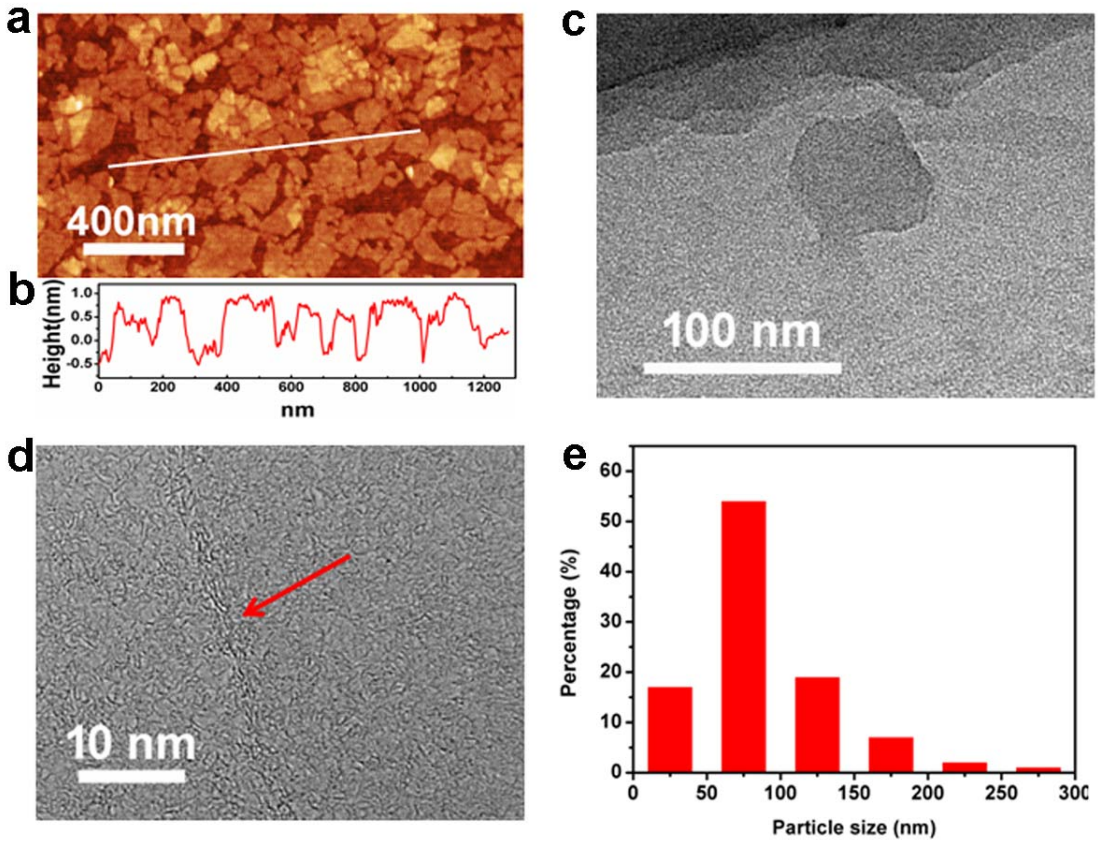

Figure S2. The characterization of NGO sheets. (a) AFM image, showing the average size of NGO is around 100 nm. (b) AFM height profile, showing the average thickness of NGO is about 1 nm. (c) TEM image of a NGO sheet, exhibiting the lateral size of 60 nm. (d) HRTEM image, demonstrating single-layer structure of NGO sheet. (e) Statistical distribution of NGO sheets based on the AFM measurement, indicating that the lateral size of~ 95% NGO sheets was less than 200 nm.

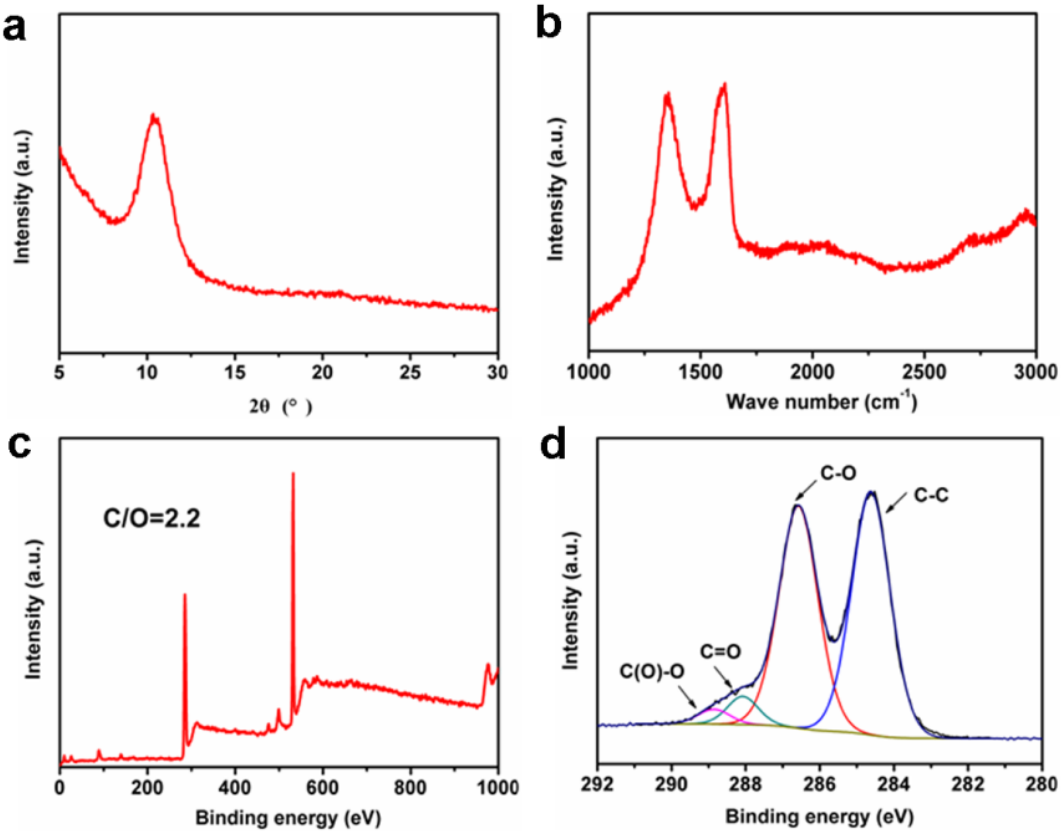

Figure S3. The structure of NGO sheets. (a) XRD pattern, showing a typical characteristic peak appearing at 10.4° with an interlayer d-spacing of 0.84 nm. (b) Raman spectrum, showing D peak at 1352 cm^{-1} and G peak at 1597 cm^{-1}. (c) XPS spectrum recorded from 0-1000 eV, exhibiting a low C/O ratio of 2.2. (d) C1s-XPS spectrum, displaying that the content of ester groups, carbonyl groups and hydroxyl or epoxide groups is approximate 2.4%, 4.5% and 45%, respectively.

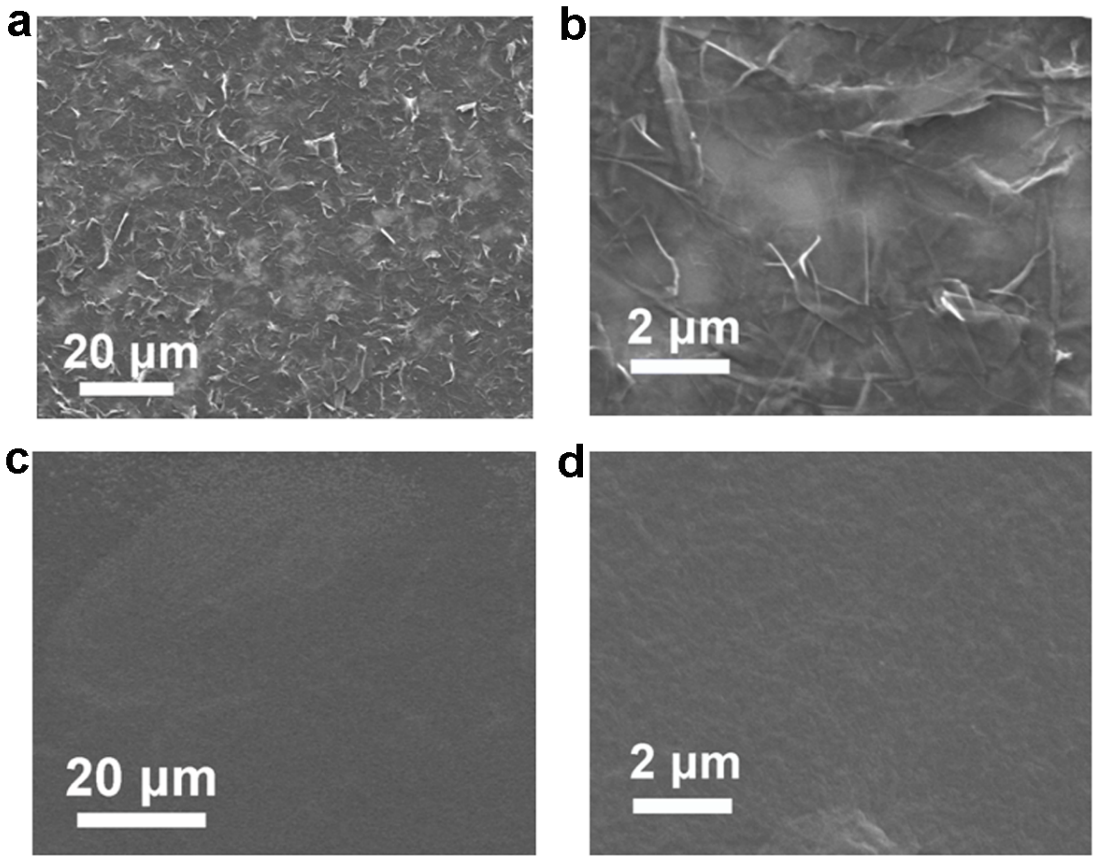

Figure S4. (a) Low-magnification and (b) high-magnification SEM images of EG layer, showing the stacked, wrinkled morphology of EG nanosheets.. (c) Low-magnification and (d) high-magnification SEM images of NGO layer, exhibiting the uniform and smooth morphology of NGO sheets.

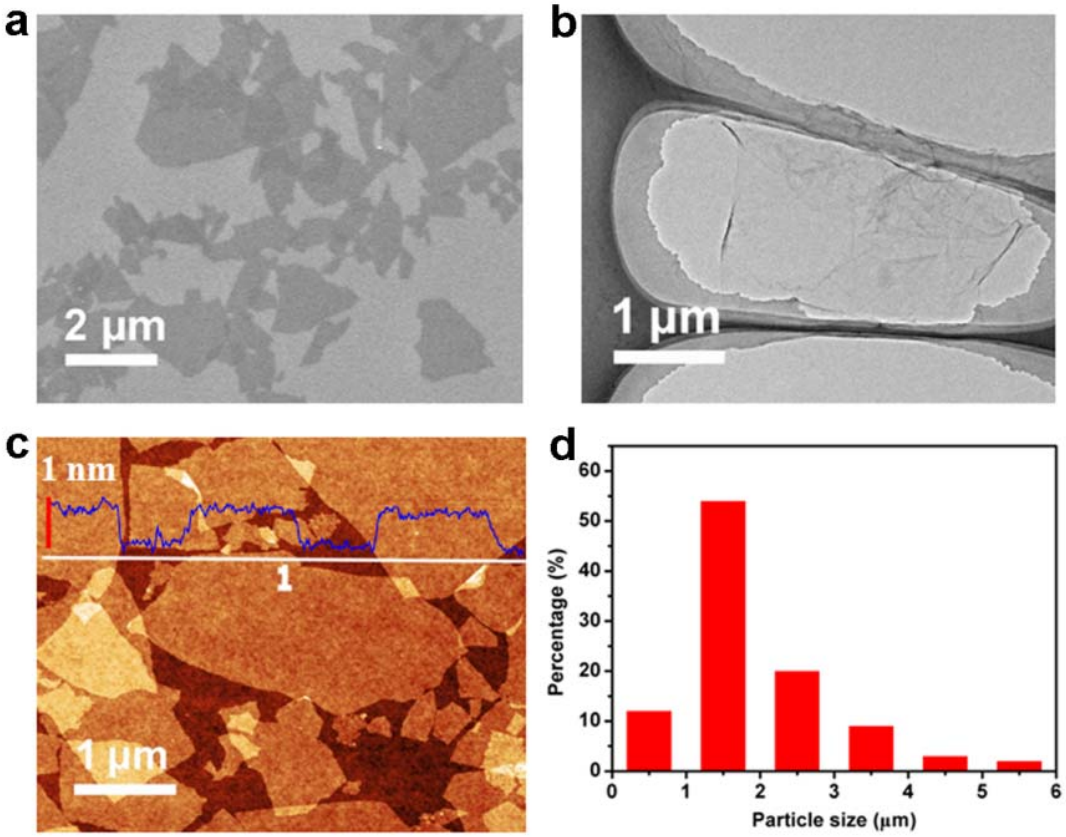

Figure S5. The characterization of GO sheets. (a) SEM image, (b) TEM image, and (c) AFM image, showing the lateral size of ~2 μm, and single-layer structure with a thickness of ~1 nm. (d) Statistical distribution of lateral size of GO sheets from AFM characterization. It is evaluated that the lateral size of GO sheets is at least one order magnitude larger than that of NGO sheets.

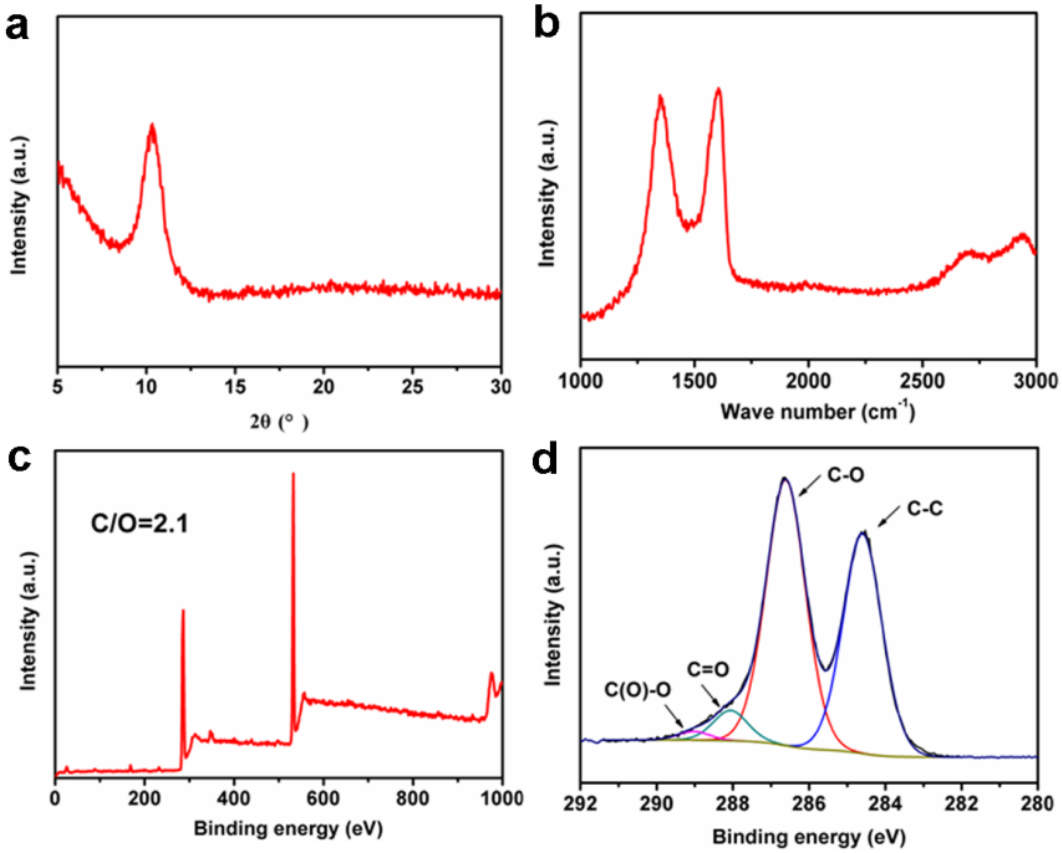

Figure S6. The structure characterization of GO sheets. (a) XRD pattern, showing a typical characteristic peak appearing at 10.4° with an interlayer d-spacing of 0.84 nm. (b) Raman spectrum, showing D peak at 1348 cm^{-1} and G peak at 1599 cm^{-1}. (c) XPS spectrum recorded from 0-1000 eV, exhibiting a low C/O ratio of 2.1. (d) C1s-XPS spectrum, displaying that the content of ester groups, carbonyl groups and hydroxyl or epoxide groups is approximate 1.3%, 5.1% and 51.5%, respectively.

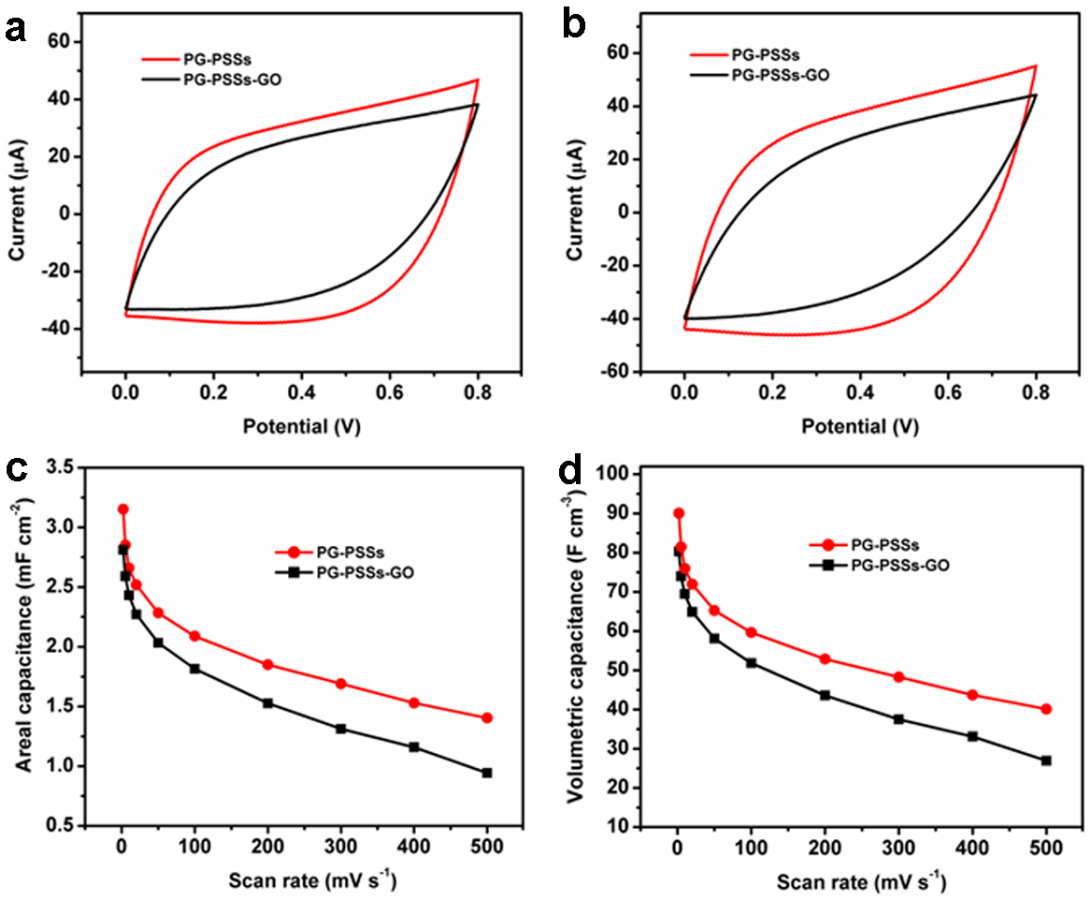

Figure S7. Performance comparison of rectangle-shaped PG-PSSs based on 350 nm-thick EG layers with NGO and GO (denoted as PG-PSSs-GO) as a separator, respectively. (a, b) CV curves at scan rates of (a) 400 mV s^{-1} and (b) 500 mV s^{-1}. It can be seen that the CV curves of PG-PSSs showed larger integration area than that of PG-PSSs-GO, indicative of higher capacitance of PG-PSSs than PG-PSSs-GO. (c) Areal capacitance and (d) volumetric capacitance of the PG-PSSs and PG-PSSs-GO as a function of scan rates from 2 to 500 mV s^{-1}, demonstrating larger specific capacitance and better rate capability of PG-PSSs with a NGO separator in comparison with PG-PSSs-GO.

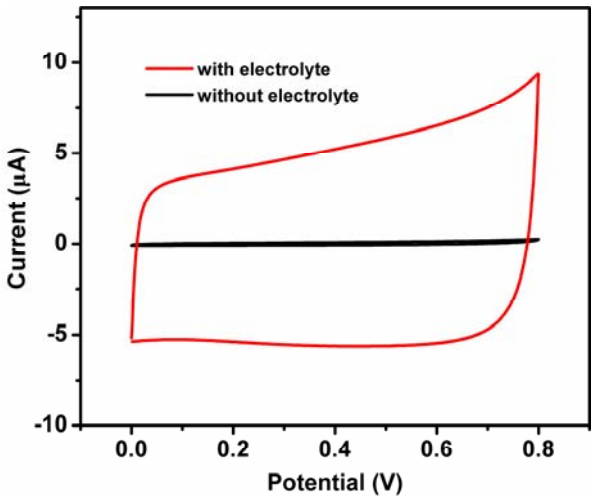

Figure S8. Performance comparison of the rectangle-shaped PG-PSSs based on a 350 nm-thick EG layer with and without electrolyte. CV curves of PG-PSSs with and without H_2SO_4/PVA gel electrolyte at a scan rate of 50 mV s^{-1}. Apparently, it is revealed that the presence of H_2SO_4/PVA gel electrolyte can greatly boost the capacitance of PG-PSSs.

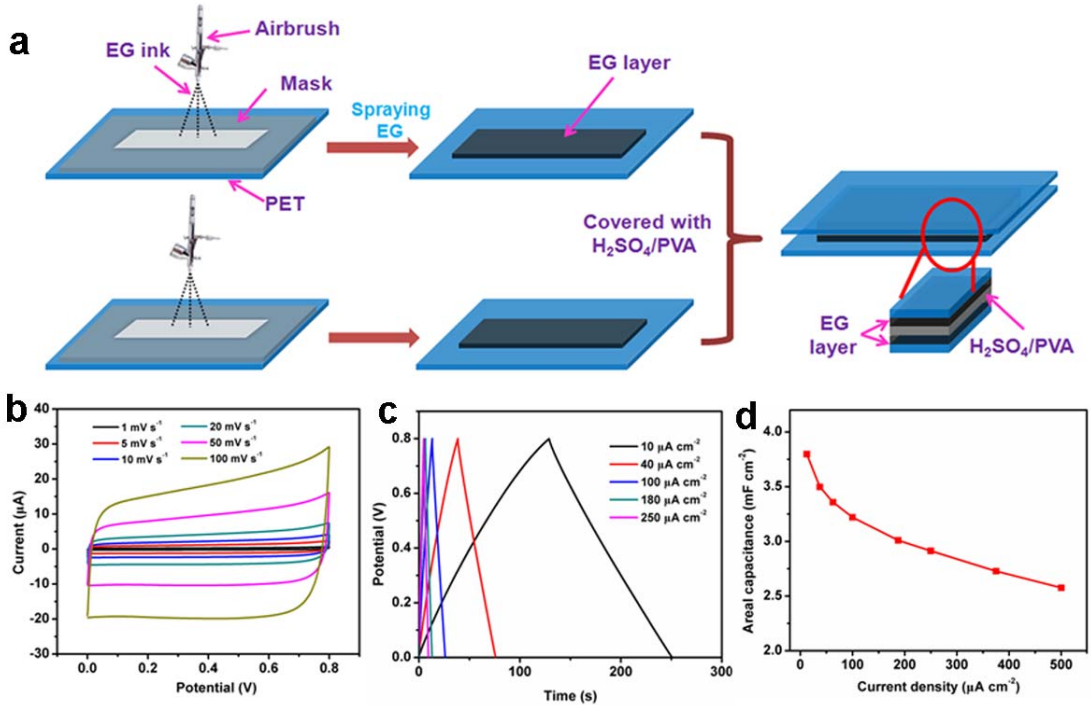

Figure S9. Schematic illustration and electrochemical characterization of rectangle-shaped PG-CSSs. (a) Schematic of the fabrication of PG-CSSs, sandwiching the H_2SO_4/PVA gel electrolyte between two same-thick EG films on PET substrates. (b) CV curves of the PG-CSSs measured at scan rates from 1 to 100 mV s^{-1}. (c) Galvanostatic charge discharge (GCD) profiles of the PG-CSSs tested at different current densities from 10 to 250 μA cm^{-2}. (d) Areal capacitance of PG-CSSs as a function of current density from 10 to 500 μA cm^{-2}.

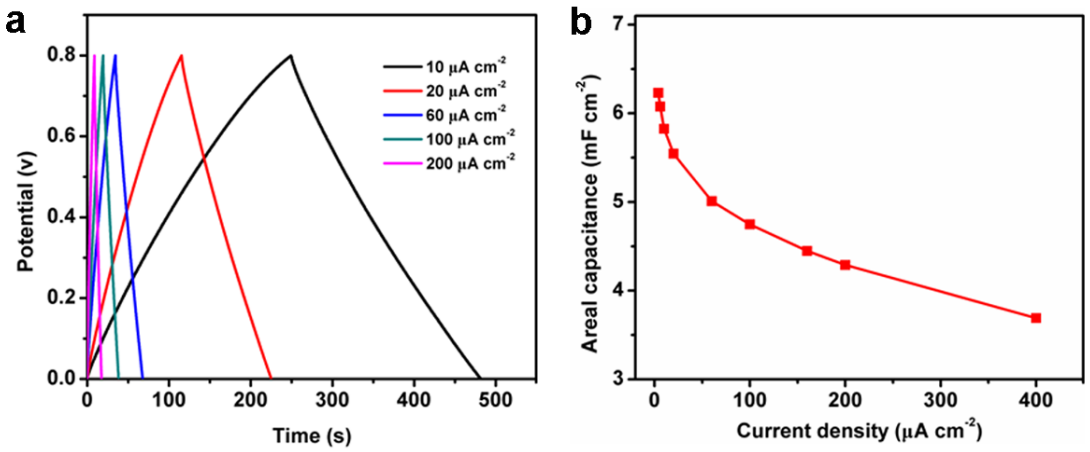

Figure S10. The GCD performance of the rectangle-shaped PG-PSSs. (a) GCD curves measured at different current densities from 10 to 200 μA cm^{-2}, showing a symmetric triangle shape, indicative of the typical electrical double layer behavior. (b) Areal capacitance of PG-PSSs as a function of current density ranging from 4 to 400 μA cm^{-2}.

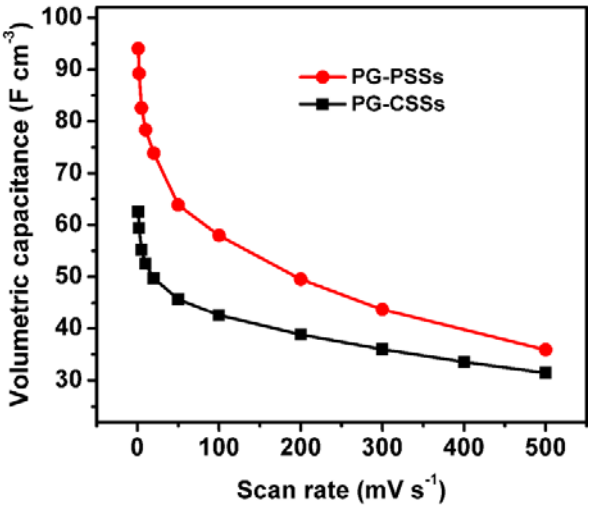

Figure S11. Performance comparison of volumetric capacitance of PG-PSSs and PG-CSSs. It can be seen that PG-PSSs exhibit higher volumetric capacitance than that of PG-CSSs.

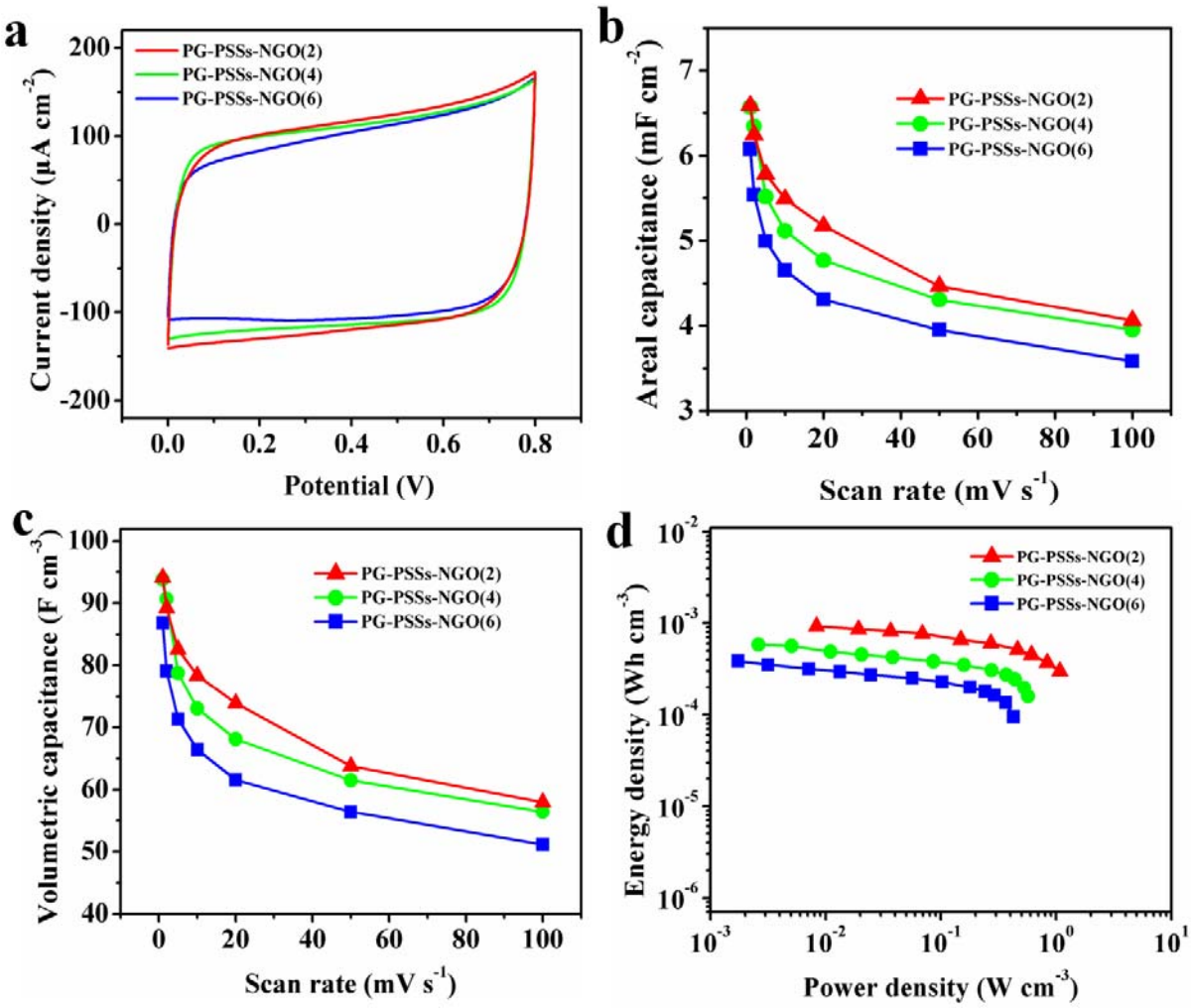

Figure S12. (a) CV curves teseted at 50 mV s^{-1}, (b) areal capacitance, (c) volumetric capacitance and (d) Ragone plots of PG-PSSs-NGO(2), PG-PSSs-NGO(4) and PG-PSSs-NGO(6), respectively.

To investigate the dependence of capacitance and power density with respect to thickness of NGO layer, we fabricated the PG-PSSs based on 2, 4, and 6 μm-thick NGO layer with the same thick EG layers, which were denoted as PG-PSSs-NGO(2), PG-PSSs-NGO(4) and PG-PSSs-NGO(6), respectively. When the thicker NGO film was used, the fabricated devices, *e.g.*, PG-PSSs-NGO(4) and PG-PSSs-NGO(6), exhibited lower capacitive responses, as indicated by the CV measurements (Figure S12a). For instance, the areal capacitance at 10 mV s^{-1} decreased from

5.5 mF cm^{-2} for PG-PSSs-NGO(2) to 5.1 mF cm^{-2} for PG-PSSs-NGO(4) and 4.7 mF cm^{-2} for PG-PSSs-NGO(6) upon increasing the NGO film thickness (Figure S12b). Further, the volumetric capacitance greatly decreased from 78.4 F cm^{-3} for PG-PSSs-NGO(2) to 73.1 F cm^{-3} for PG-PSSs-NGO(4) and 66.4 F cm^{-3} for PG-PSSs-NGO(6) (Figure S12c) at 10 mV s^{-1}. More importantly, Ragone plots calculated based on the device further revealed that the PG-PSSs-NGO(2) with thinner NGO layer delivered higher power density and energy density than PG-PSSs-NGO(4) and PG-PSSs-NGO(6), as shown in Figure S12d. For example, PG-PSSs-NGO(2) presented a large power density of 1.1 W cm^{-3}, which was much higher than those of PG-PSSs-NGO(4) (0.6 W cm^{-3}) and PG-PSSs-NGO(6) (0.4 W cm^{-3}).

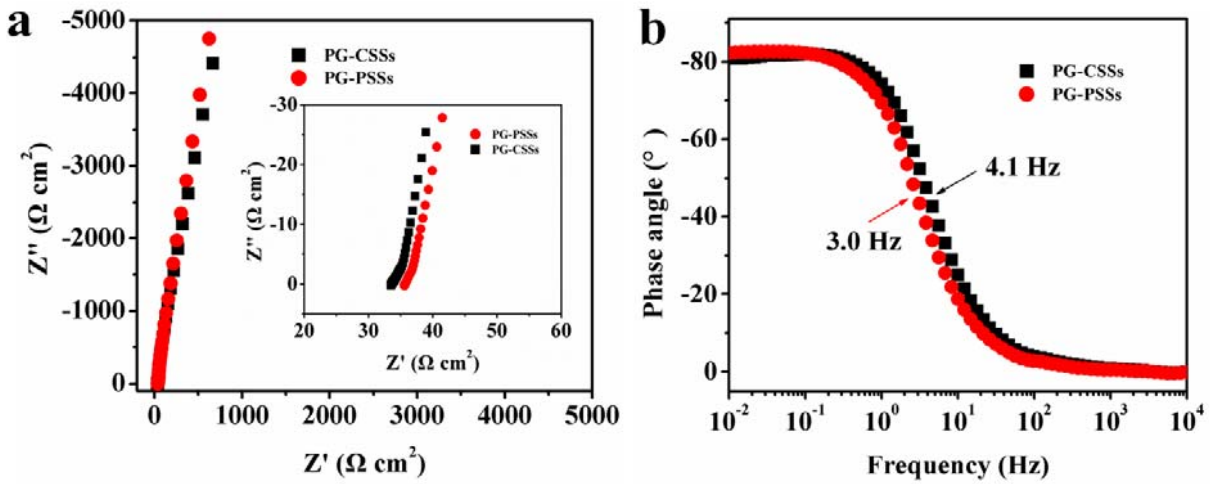

Figure S13. (a) Complex plane plots of the impedance of PG-PSSs and PG-CSSs. Inset is the magnified plots of the high-frequency region. (b) Impedance phase angle as a function of frequency of PG-PSSs and PG-CSSs.

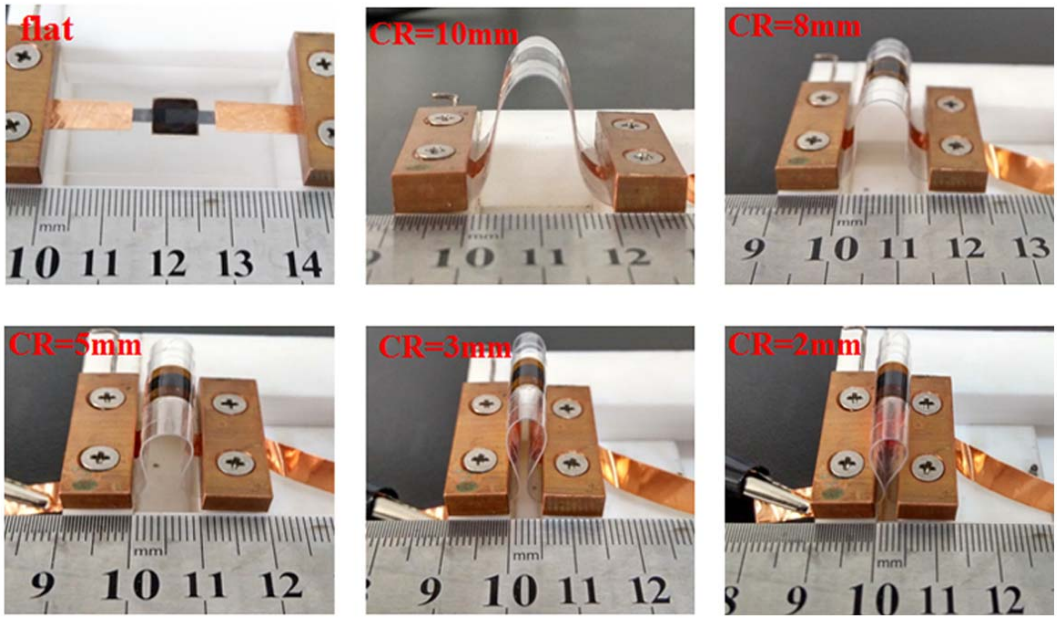

Figure S14. Optical images of the rectangle-shaped PG-PSSs at flat and bent states with different curvature radius (CR), showing the excellent mechanical flexibility.

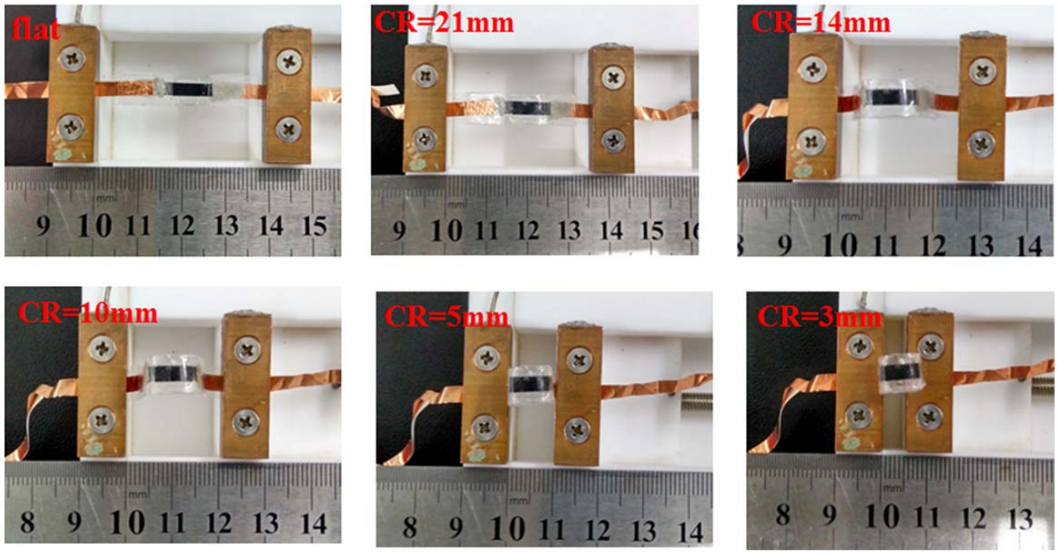

Figure S15. Optical images of the rectangle-shaped PG-CSSs at flat and bent states with different curvature radius.

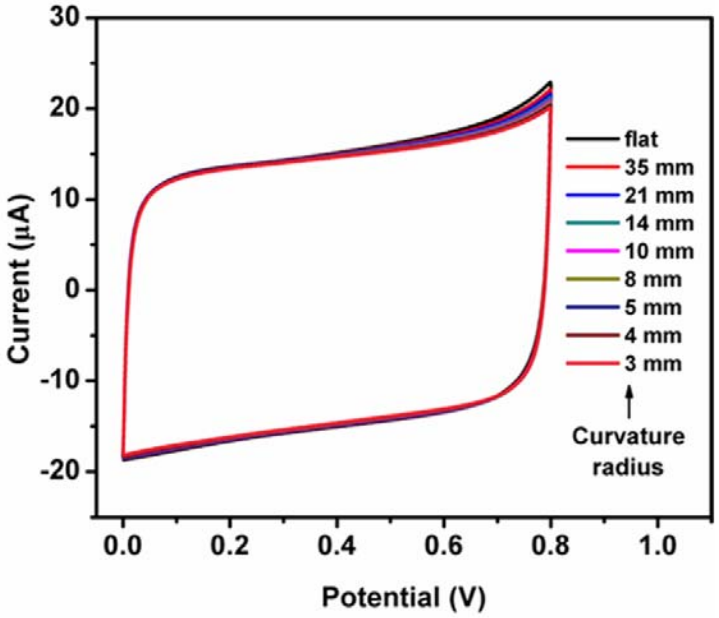

Figure S16. CV curves of the rectangle-shaped PG-CSSs at flat and bent states with different curvature radius measured at the scan rate of 50 mV s^{-1}. It is observed that at a curvature radius of 3 mm, the PG-CSSs retained 95% of the initial capacitance at a flat state.

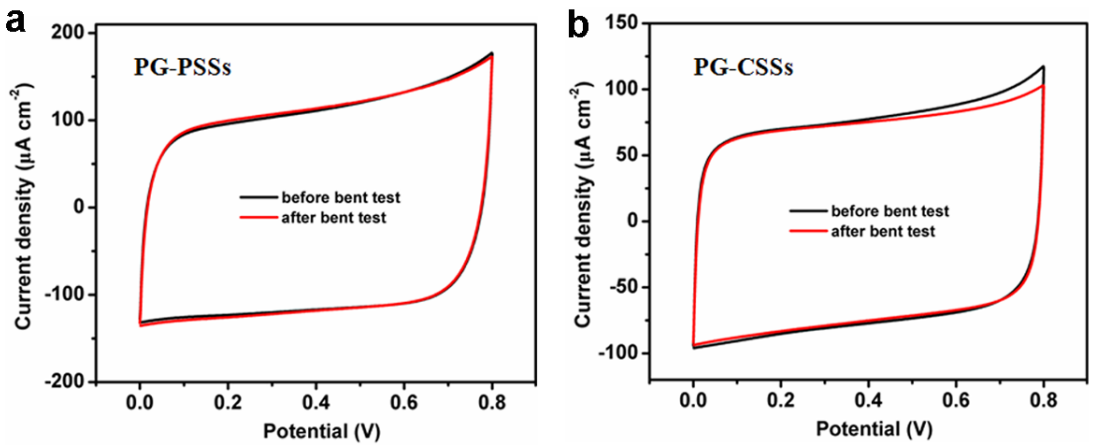

Figure S17. CV curves of the rectangle-shaped PG-PSSs and PG-CSSs before and after bending test. (a, b) The CV curves of (a) PG-PSSs and (b) PG-CSSs obtained at a scan rate of 50 mV s^{-1} before and after the bending test. No capacitance loss was observed for the PG-PSSs while about ~5% capacitance degradation was revealed for the PG-CSSs, demonstrative of the configuration superiority of PG-PSSs over PG-CSSs.

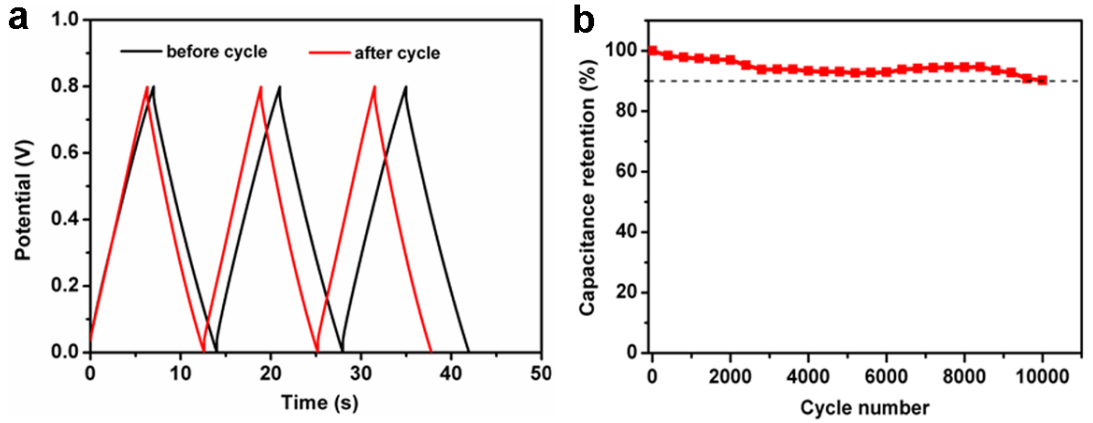

Figure S18. Cycling stability of the rectangle-shaped PG-CSSs. (a) GCD curves of the PG-CSSs before and after 10000 cycles. (b) The capacitance retention of the PG-CSSs measured at current density of 250 μA cm^{-2} with 90.1% capacitance retention after 10000 cycles. Obviously, this value is lower than that of PG-PSSs (~93.4%).

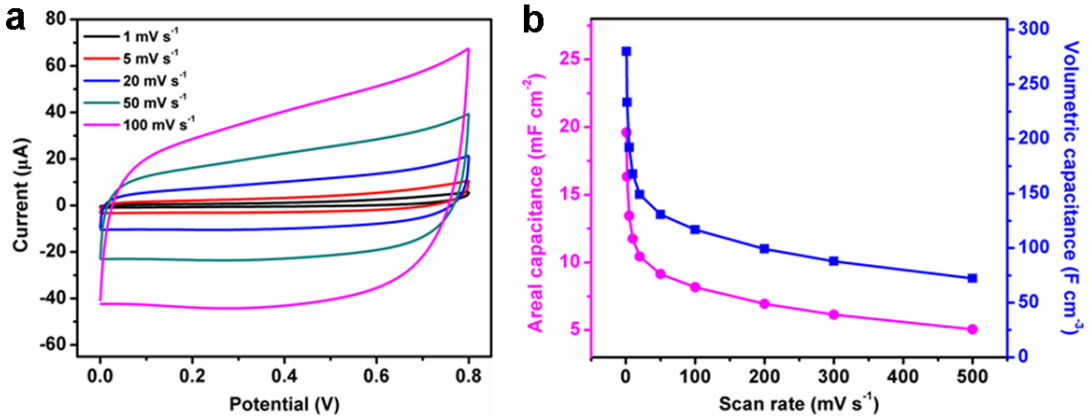

Figure S19. The electrochemical performance of the rectangle-shape PG/HQ-PSSs. (a) CV curves measured at scan rate from 1 to 100 mV s^{-1}. (b) Areal and volumetric capacitance of PG/HQ-PSSs. It is noted that the areal and volumetric capacitance is 19.6 mF cm^{-2} and 280 F cm^{-3} obtained at 1 mV s^{-1}, respectively, which are three times higher than those of PG-PSSs.

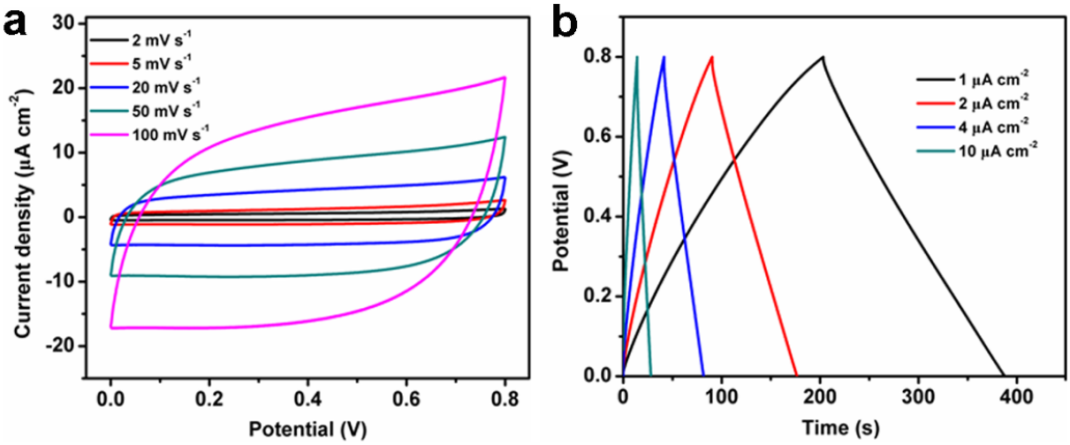

Figure S20. Electrochemical performance of the hollow-square-shaped PG-PSSs based on ~70 nm-thick EG films. (a) CV curves obtained at scan rates from 2 to 100 mV s^{-1}. (b) GCD profiles measured at current densities from 1 to 10 μA cm^{-2}.

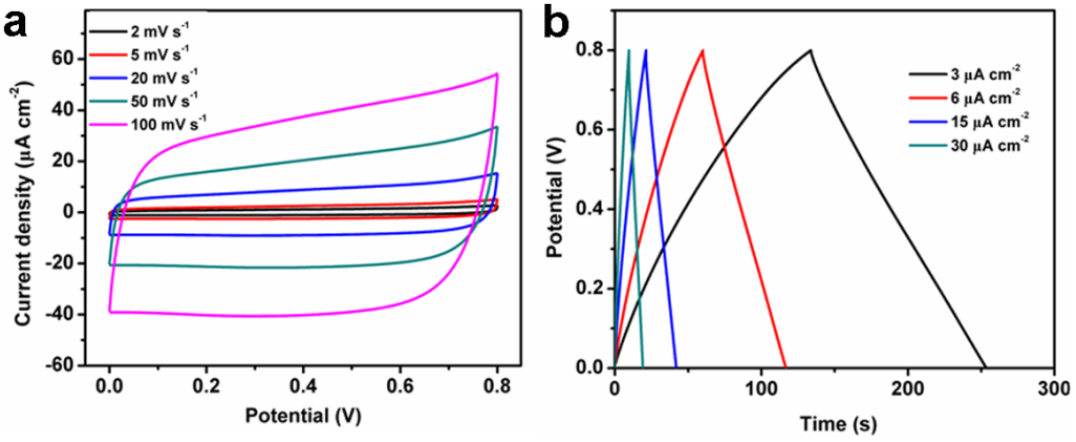

Figure S21. Electrochemical performance of the "**A**"-shaped PG-PSSs based on ~100 nm-thick EG layers. (a) CV curves obtained at scan rates from 2 to 100 mV s^{-1}. (b) GCD profiles tested at current densities from 3 to 30 μA cm^{-2}.

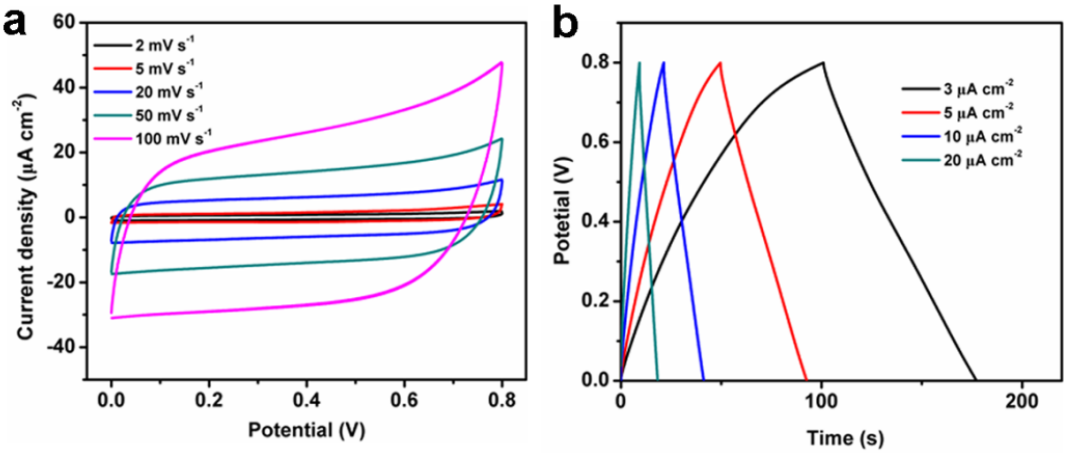

Figure S22. Electrochemical performance of the "**1**"-shaped PG-PSSs based on ~80 nm-thick EG layers. (a) CV curves obtained at scan rates from 2 to 100 mV s^{-1}. (b) GCD curves measured at current densities from 3 to 20 μA cm^{-2}.

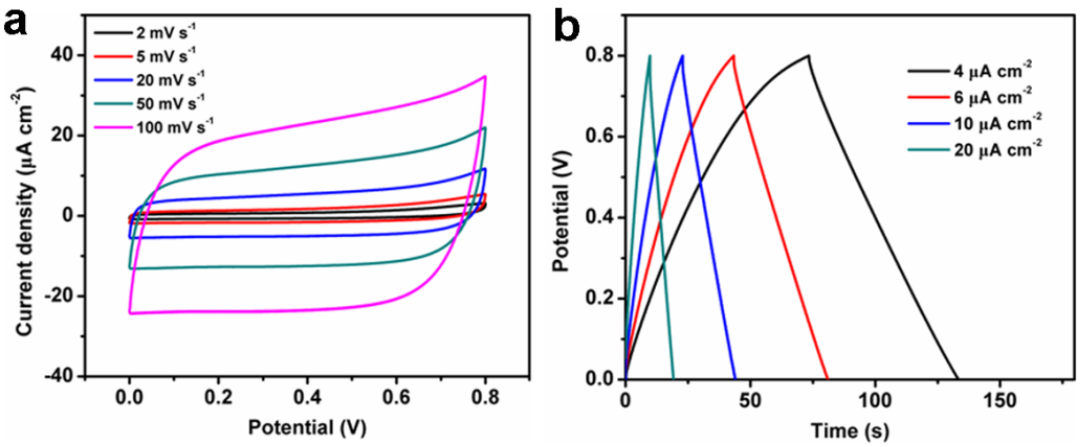

Figure S23. The electrochemical performance of the "**2**"-shaped PG-PSSs based on ~100 nm-thick EG layers. (a) CV curves measured at scan rate from 2 to 100 mV s^{-1}. (b) GCD profiles obtained at current densities from 4 to 20 μA cm^{-2}.

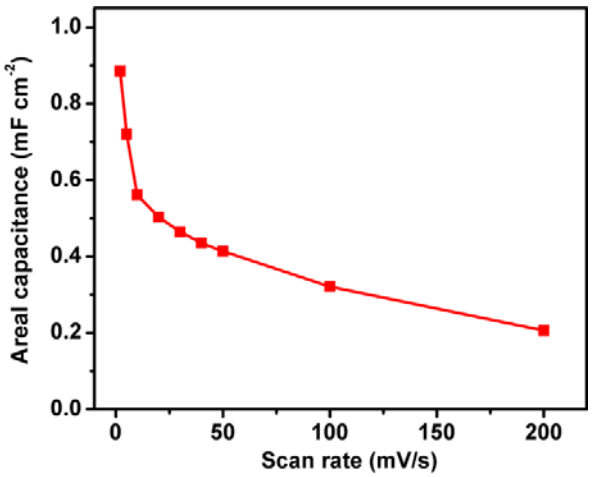

Figure S24. Areal capacitance of the junction-wire-shaped PG-PSSs based on ~90 nm-thick EG layers at scan rates from 2 to 200 mV s^{-1}.

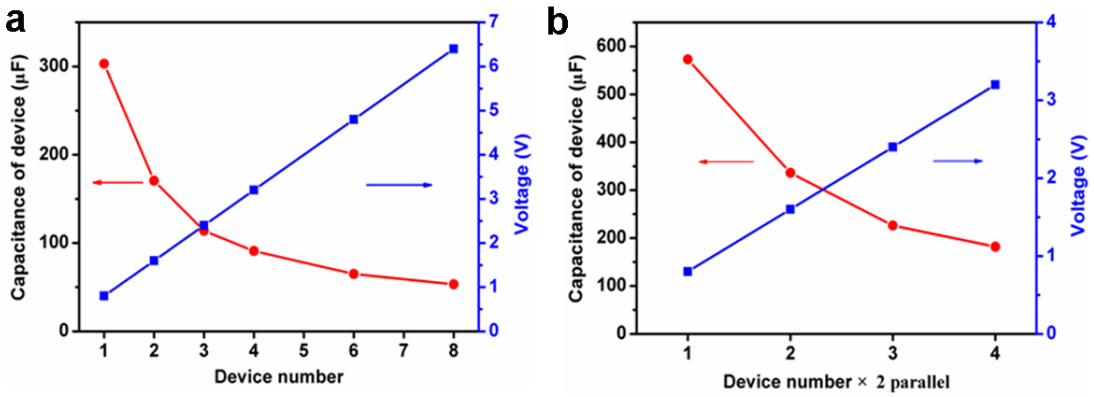

Figure S25. The capacitance of serial and parallel circle-shaped PG-PSSs obtained at the scan rate of 50 mV s^{-1}. (a) Plot of capacitance and voltage versus the number of the serial cells. (b) Plot of capacitance and voltage versus the number of the serial and 2 parallel cells.

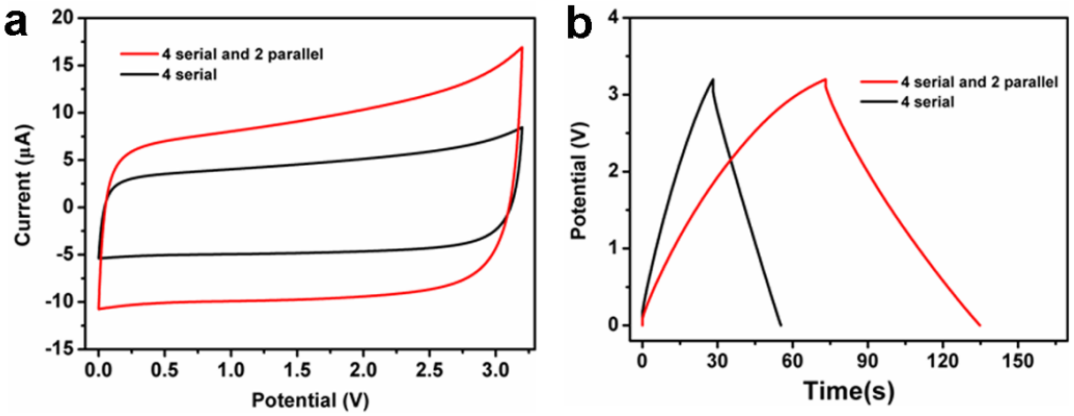

Figure S26. Electrochemical performance of serial and parallel circle-shaped PG-PSSs. (a) CV curves obtained at scan rate of 50 mV s^{-1} and (b) GCD profiles tested at current density 20 μA cm^{-2} of 4 serial PG-PSS pack and 4 serial and 2 parallel PG-PSS pack, demonstrating the simultaneous enhancement of both capacitance and voltage.

Table S1. Comparison of electrochemical performance of the state-of-the-art graphene-based planar supercapacitors

Supercapacitors	Electrolyte	Thickness (μm)	C_{device}^{areal} (mF cm^{-2})	$C_{device}^{volumetric}$ (F cm^{-3})	P_{device} (mW cm^{-3})	E_{device} (mWh cm^{-3})	Refs.
LWG-MSCs	H_2O-excess	1.6	0.51	3.1	1700	0.43	1
LSG-SSCs	PVA/H_2SO_4	7.6	3.67	5.1	2000	0.7	2
	$EMIMBF_4$		5.02	0.6	20000	1.36	
LSG-SSCs	PVA/H_2SO_4	7.6		0.85	7000	0.12	3
	Ionic liquid			0.7	20000	0.6	
LSG-MSCs	PVA/H_2SO_4		2.32	3.05	70000	0.42	
	Ionic liquid			2.35	200000	2	
GCNTC-MSCs	Na_2SO_4	10	2.16	1.08	30000	0.15	4
LIPG-MSCs	H_2SO_4	25		1.5		0.21	5
B-LIG-MSCs	PVA/H_2SO_4	25	16.5	4.3	2000	0.6	6
LIG -SSCs	PVA/H_2SO_4	25	9	3.6	300	0.5	7
rGO/CNT-MSCs	KCl	6	6.1		77000	0.7	8
rGO/GO/rGO -SSCs	GO	10	2		120	0.11	9
CGF-SSCs	PVA/H_3PO_4	12.6	56.8	7.9	10000	1.1	10
LPG-MSCs	PVA/LiCl	6	3.9	8.7	2000	0.98	11
PG-PSSs	PVA/H_2SO_4	0.7	3.3	10.6	2100	0.98	This
PG/HQ-PSSs	PVA/H_2SO_4	0.7	9.8	32.7	2340	2.9	work

MSCs: micro-supercapacitors; SSCs: sandwich supercapacitors; LWG: laser-written graphene; LSG: laser scribed graphene; GCNTC: graphene carbon nanotube carpet; LIPG:laser-induced porous graphene; B-LIG: B-doped laser induced graphene; LIG:laser induced graphene ; CNT: carbon nanotube ;GO: graphene oxide; rGO: reduced graphene oxide; GCF:cellular graphene film**;** LPG:laser-processed graphene

Table S2. The length and width parameters of PG-PSSs with different shapes (left), and the specific dimensions of mask 1 and mask 2 for the designed circle-shaped PG-PSSs (right).

Shapes	Length (mm)		Width (mm)	
	EG	NGO	EG	NGO
rectangle	10	8	3	8
one side of hollow-square	6	7	1	2.5
"A"	13	16	1	2.5
"1"	11	12	1	2.5
"2"	15	18	1	2.5
junction-wire	46	50	1.2	2

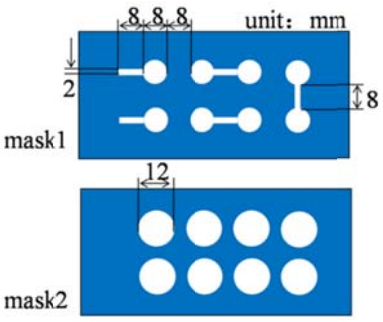

Calculation of the Performance Parameters

The capacitance of the fabricated devices was calculated from the discharged CV curves according to the following equation (1):

$$C = \frac{1}{v(V_f - V_i)} \int_{V_i}^{V_f} I(V)dV \qquad (1)$$

Where $I(V)$ is the discharging current (A), V_f and V_i are the integration potential limitation of the voltammetric curves and ν is the scan rate (V s^{-1}).

Specific capacitances of the EG film electrode were calculated based on area and volume of single electrode according to the following equations (2) and (3) :

$$C_{electrode}^{areal} = 4 \times C / A_{electrode} \qquad (2)$$

$$C_{electrode}^{volumetric} = 4 \times C / V_{electrode} \qquad (3)$$

Where $A_{electrode}$ (cm^2) and $V_{electrode}$ (cm^3) represent the area and volume of two electrodes, respectively. $C_{electrode}^{areal}$ (F cm^{-2}) and $C_{electrode}^{volumetric}$ (F cm^{-3}) refer to the areal and volumetric capacitance of the single electrode, respectively.

Specific capacitances of the devices were calculated based on area and volume of the device according to the following formula (4) and (5):

$$C_{device}^{areal} = C / A_{device} \quad (4)$$

$$C_{device}^{volumetric} = C / V_{device} \quad (5)$$

Where A_{device} (cm^2) and V_{device} (cm^3) represent the total area and volume of the device, respectively. $C_{\text{device}}^{areal}$ (F cm^{-2}) and $C_{device}^{volumetric}$ (F cm^{-3}) refer to the areal and volumetric capacitance of the device, respectively. The volume of device include the active material, gel electrolyte and separator.

The volumetric energy density and power density of the devices were calculated from the following equations (6) and (7):

$$E = \frac{1}{2} \times C_{device}^{volumetric} \times \frac{(\Delta V)^2}{3600} \quad (6)$$

$$P = \frac{E}{\Delta t} \times 3600 \quad (7)$$

where E is the volumetric energy density (Wh cm^{-3}), and P is the volumetric power density (W cm^{-3}). ΔV is the discharge voltage (V), and Δt is the discharge time (s).

References

(1). Gao, W.; Singh, N.; Song, L.; Liu, Z.; Reddy, A. L. M.; Ci, L. J.; Vajtai, R.; Zhang, Q.; Wei, B. Q.; Ajayan, P. M. Direct Laser Writing of Micro-Supercapacitors on Hydrated Graphite Oxide Films. *Nat. Nanotechnol.* **2011,** *6*, 496-500.

(2). El-Kady, M. F.; Strong, V.; Dubin, S.; Kaner, R. B. Laser Scribing of High-Performance and Flexible Graphene-Based Electrochemical Capacitors. *Science* **2012,** *335*, 1326-1330.

(3). El-Kady, M. F.; Kaner, R. B. Scalable Fabrication of High-Power Graphene Micro-Supercapacitors for Flexible and on-Chip Energy Storage. *Nat. Commun.* **2013,** *4*. 1475.

(4). Lin, J.; Zhang, C.; Yan, Z.; Zhu, Y.; Peng, Z.; Hauge, R. H.; Natelson, D.; Tour, J. M. 3-Dimensional Graphene Carbon Nanotube Carpet-Based Microsupercapacitors with High Electrochemical Performance. *Nano Lett.* **2013,** *13*, 72-78.

(5). Lin, J.; Peng, Z.; Liu, Y.; Ruiz-Zepeda, F.; Ye, R.; Samuel, E. L. G.; Yacaman, M. J.; Yakobson, B. I.; Tour, J. M. Laser-Induced Porous Graphene Films from Commercial Polymers. *Nat. Commun.* **2014,** *5*, 5714.

(6). Peng, Z.; Ye, R.; Mann, J. A.; Zakhidov, D.; Li, Y.; Smalley, P. R.; Lin, J.; Tour, J. M. Flexible Boron-Doped Laser-Induced Graphene Microsupercapacitors. *ACS Nano* **2015,** *9*, 5868-5875.

(7). Peng, Z.; Lin, J.; Ye, R.; Samuel, E. L. G.; Tour, J. M. Flexible and Stackable Laser-Induced Graphene Supercapacitors. *ACS Appl. Mater. Interfaces* **2015,** *7*, 3414-3419.

(8). Beidaghi, M.; Wang, C. Micro-Supercapacitors Based on Interdigital Electrodes of Reduced Graphene Oxide and Carbon Nanotube Composites with Ultrahigh Power Handling Performance. *Adv. Funct. Mater.* **2012,** *22*, 4501-4510.

(9). Ogata, C.; Kurogi, R.; Hatakeyama, K.; Taniguchi, T.; Koinuma, M.; Matsumoto, Y. All-Graphene Oxide Device with Tunable Supercapacitor and Battery Behaviour by The Working Voltage. *Chem. Commun.* **2016,** *52*, 3919-3922.

(10). Shao, Y.; El-Kady, M. F.; Lin, C.-W.; Zhu, G.; Marsh, K. L.; Hwang, J. Y.; Zhang, Q.; Li, Y.; Wang, H.; Kaner, R. B. 3D Freeze-Casting of Cellular Graphene Films for Ultrahigh-Power-Density Supercapacitors. *Adv. Mater.* **2016,** *28*, 6719-6726.

(11). Xie, B.; Wang, Y.; Lai, W.; Lin, W.; Lin, Z.; Zhang, Z.; Zou, P.; Xu, Y.; Zhou, S.; Yang, C.; Kang, F.; Wong, C.-P. Laser-Processed Graphene Based Micro-Supercapacitors for Ultrathin, Rollable, Compact and Designable Energy Storage Components. *Nano Energy* **2016,** *26*, 276-285.